Observing—and Imaging—Active Galactic Nuclei with the Event Horizon Telescope

Vincent L. Fish [1,*], Kazunori Akiyama [1,2], Katherine L. Bouman [3], Andrew A. Chael [4], Michael D. Johnson [4], Sheperd S. Doeleman [4], Lindy Blackburn [4], John F. C. Wardle [5], William T. Freeman [3,6] and the Event Horizon Telescope Collaboration

[1] Massachusetts Institute of Technology, Haystack Observatory, Westford, MA 01886, USA; kazu@haystack.mit.edu

[2] Japan Society for the Promotion of Science, Chiyoda (Tokyo) 102-0083, Japan

[3] Massachusetts Institute of Technology, Computer Science and Artificial Intelligence Laboratory, Cambridge, MA 02139, USA; klbouman@mit.edu (K.L.B.); billf@mit.edu (W.T.F.)

[4] Harvard-Smithsonian Center for Astrophysics, Cambridge, MA 02138, USA; achael@physics.harvard.edu (A.A.C.); mjohnson@cfa.harvard.edu (M.D.J.); sdoeleman@cfa.harvard.edu (S.S.D.); lblackburn@cfa.harvard.edu (L.B.)

[5] Physics Department, Brandeis University, Waltham, MA 02453, USA; wardle@brandeis.edu

[6] Google Inc., 1600 Amphitheatre Parkway, Mountain View, CA 94043, USA

* Correspondence: vfish@haystack.mit.edu; Tel.: +1-781-981-5400

Abstract: Originally developed to image the shadow region of the central black hole in Sagittarius A* and in the nearby galaxy M87, the Event Horizon Telescope (EHT) provides deep, very high angular resolution data on other active galactic nucleus (AGN) sources too. The challenges of working with EHT data have spurred the development of new image reconstruction algorithms. This work briefly reviews the status of the EHT and its utility for observing AGN sources, with emphasis on novel imaging techniques that offer the promise of better reconstructions at 1.3 mm and other wavelengths.

Keywords: galaxies: jets; galaxy: center; techniques: high angular resolution; techniques: image processing; techniques: interferometric

1. The Event Horizon Telescope

1.1. Overview

The Event Horizon Telescope (EHT) is a very long baseline interferometry (VLBI) array currently operating at a wavelength of 1.3 mm, with an extension to 0.87 mm to come. A primary goal of the EHT is to observe and image supermassive black holes with enough angular resolution to study the innermost accretion and outflow region at a few gravitational radii from the black hole [1].

The EHT consists of millimeter/submillimeter telescopes scattered across the globe, including the Submillimeter Array and James Clerk Maxwell Telescope in Hawaii, the Submillimeter Telescope on Mt. Graham in Arizona, the Large Millimeter Telescope in Mexico, the Atacama Pathfinder Experiment in Chile, the South Pole Telescope, the Institut de radioastronomie millimétrique (IRAM) 30-m telescope on Pico Veleta in Spain, and the IRAM Plateau de Bure Interferometer in France (currently being upgraded as part of the Northern Extended Millimeter Array project). A beamformer has been built for the Atacama Large Millimeter/submillimeter Array (ALMA) to allow it to operate as a very sensitive single aperture for VLBI. Several other observatories have participated in previous EHT observations, and additional observatories are on track to join the array in upcoming years.

The angular resolution of the EHT is especially well matched to the scale of emission in the black holes in the center of the Milky Way (known as Sagittarius A* or Sgr A*) and the giant elliptical galaxy M87. General relativity predicts that if a black hole is surrounded by optically thin emission, the black hole will cast an approximately circular shadow with a diameter of around 10 gravitational radii (1 $r_g = GMc^{-2}$), which corresponds to about 50 μas in Sgr A* and 40 μas in M87. Fringe spacings of EHT baselines at 1.3 mm span a range of approximately 25 to 300 μas, providing both the resolution needed to image the shadow region and shorter spacings to be sensitive to the accretion and outflow region out to a few tens of r_g. The very high angular resolution of the EHT is also useful for studying compact structures in other AGN sources. For instance, EHT observations of the quasars J1924−2914 and 3C 279 have demonstrated that the small structures seen at 1.3 mm have lower brightness temperatures than seen at centimeter wavelengths [2–4].

1.2. Key Science Results on Sgr A and M87*

Sgr A* has been routinely detected on long EHT baselines since 2007, and M87 since 2009. Although early EHT experiments have not had the sensitivity or baseline coverage to directly reconstruct images of these targets or other sources, a large number of important scientific results have been derived from the visibility data obtained to date. A very brief summary of these results appears below, with full details to be found in the referenced papers.

- The 1.3 mm emission regions in Sgr A* and M87 have an effective size of only a few r_g [5,6].
- The small sizes of Sgr A* and M87 combined with their relatively weak infrared emission make a very strong case that these sources have an event horizon and are therefore black holes [7,8].
- The millimeter-wavelength emission region in Sgr A* remains compact when the source flares [9].
- Sgr A* is asymmetric on angular scales comparable to the shadow diameter. This asymmetry is persistent and intrinsic to the source, rather than arising from the foreground scattering screen [10].
- The magnetic field in the inner accretion flow around Sgr A* is partially ordered. The polarized millimeter-wavelength flux arises from the same region as the total intensity during quiescence, but polarized variability can occur in regions that are offset from the main emission region [11].
- The data strongly constrain specific model classes for Sgr A* and M87. In most cases, these models find that the black hole spin vector is inclined significantly with respect to the line of sight [12–15].
- The consistency of the size of the millimeter-wavelength emission in M87 before and during a very high energy flare favors models in which γ rays originate in an extended region [16].

1.3. Observing AGN Sources with the EHT

The EHT is uniquely capable of probing the innermost regions of other AGN sources at high angular resolution. The EHT penetrates more deeply into the synchrotron photosphere of jets than any other, lower-frequency VLBI array. With an angular resolution of better than 25 μas, the EHT provides superior resolving power on AGN sources, which is exceeded only by RadioAstron—and even then only at greatest elongation, at its highest frequency (22 GHz, a factor of 10 smaller than the EHT), and typically only in a single direction in an observing epoch (although its evolving orbit allows different directions to be sampled at different times) [17]. The combination of high angular resolution and high frequency allows the EHT to measure jet widths much closer to the launch point than lower-frequency observations, enabling detailed studies of the inner collimation region. As a high-frequency, wide-bandwidth observing array, the EHT will also be able to detect and measure regions of high rotation measure in jet sources [18]. With the expansion of the EHT to a total data rate of 64 Gb s^{-1} split across two noncontiguous sidebands, the spanned frequency will be large enough to study sources with high rotation measures, such as 3C 84 [19].

The range of scientific projects that can be undertaken with the EHT is very large [20,21]. The ALMA Phasing Project has created a beamformer for ALMA, which enhances the sensitivity of the EHT array and thus greatly extends the range of sources that can be observed with the EHT. As part of the ALMA Cycle 4 Call for Proposals, the ALMA phasing system was for the first time offered for open-access VLBI observing in conjunction with the EHT at 1.3 mm and the Global mm-VLBI Array (GMVA) at 3.5 mm. Inclusion of ALMA also extends the north-south resolution of these VLBI arrays (Figure 1). Thanks to the increases in sensitivity and baseline coverage, VLBI arrays that make use of phased ALMA will be able to make better images than have heretofore been possible.
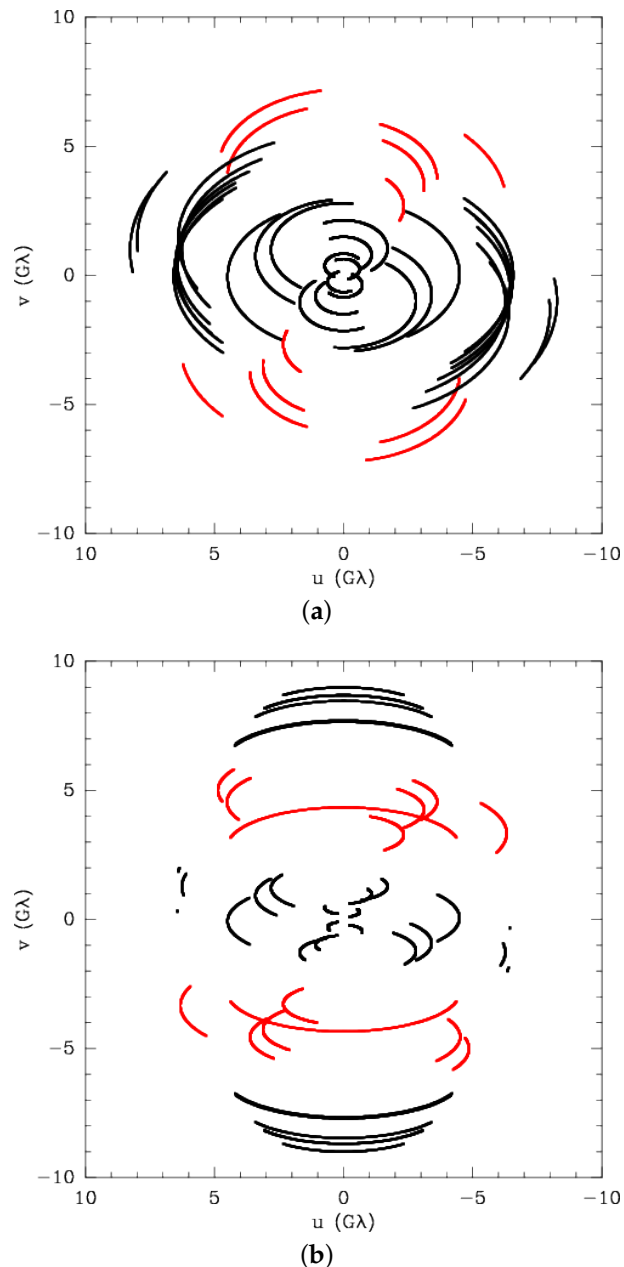

(a)

(b)

Figure 1. Event Horizon Telescope (EHT) 1.3 mm baseline coverage for a source at $+40°$ declination (**a**) and $-20°$ (**b**). Baselines to Atacama Large Millimeter/submillimeter Array (ALMA) are shown in red. ALMA baselines extend north-south coverage and are especially important for southern sources, where they fill in a large gap in the (u, v) plane between the intra–northern hemisphere baselines and the very long baselines to the South Pole Telescope.

2. Imaging

Reconstructing an image of the observed target is a critical part of VLBI observing, no matter which array is used or which frequency is observed. VLBI arrays generally sample the (u, v) plane only sparsely, leaving many Fourier components of the sky image unsampled. Image reconstruction methods make use of the limited data (e.g., measured visibilities) along with externally imposed constraints (e.g., positive definiteness in Stokes I images) to select one image out of the many that are consistent with the data.

2.1. Traditional Imaging Algorithm: CLEAN

The most commonly used image reconstruction algorithm for radio interferometer data is CLEAN [22]. Visibilities are gridded and Fourier transformed to produce a dirty map that is contaminated by the sidelobe structure of the dirty beam. To remove the sidelobe structure, CLEAN runs an iterative loop in which the dirty beam is recentered at the brightest pixel in the dirty map and a fraction of the brightness of that pixel, along with its sidelobe contribution to other pixels, is subtracted. This loop is run until an end condition is reached, typically determined by the number of loop iterations, the noise level in the residual map, or the effective dynamic range of the image. The CLEAN components are then convolved with a restoring beam and added back to the residual map.

In the many years since CLEAN was introduced, numerous variants of the algorithm have been implemented to optimize for speed, suppress artifacts, handle extended sources, image wide fields, and deal with spectral structure across wide bandwidths [23–26]. All of these variations use deconvolution to remove the dirty beam structure from the dirty map. CLEAN variants have become very popular in radio interferometry, due both to their success in producing reasonable images from most radio arrays and to their implementation in common radio interferometry data reduction packages, such as AIPS, CASA, and Miriad.

2.2. Limitations of CLEAN for Imaging with the EHT

CLEAN has been successful in producing interferometric images of adequate quality at lower frequencies. However, it is less well suited to reconstructing images from the EHT for several reasons.

First, the (u, v) coverage of the EHT is sparse due to the limited number of observatory sites and their distribution on the Earth. The resulting dirty beam of the EHT has large sidelobes, which can lead to large artifacts in images reconstructed by CLEAN.

Second, the fundamental VLBI observable used by CLEAN is the (calibrated) complex visibility on each baseline in each Stokes parameter. Rapidly varying tropospheric delays preclude phase-calibration of the data via the technique of nodding between the target source and a nearby calibrator. The EHT compensates for this by using robust VLBI quantities where possible. The robust Stokes I phase observable is the closure phase, which is the directed sum of visibility phases around a closed triangle of stations (or equivalently, the phase of the bispectrum, which is the product of the three complex visibilities) [27,28]. When possible, it is also preferable to use closure amplitudes—ratios of visibility amplitudes among quadrangles of stations—that are less sensitive to gain fluctuations at each antenna. For linear polarization, it is most natural to use complex polarimetric ratios such as RL/LL, where L and R refer to the left and right circular polarizations, which are robust against both atmospheric phase variations and gain fluctuations [29]. Hybrid mapping can use CLEAN to incorporate closure information into station-based complex gains, but it is preferable to work with the robust observables directly.

Third, the effective angular resolution provided by CLEAN is coarser than that provided by, e.g., the Maximum Entropy Method (MEM) [30]. The diameters of the predicted black hole shadows in Sgr A* and M87 are only approximately twice the fringe spacing of the longest baselines at 1.3 mm. This is sufficient for producing an image of the shadow region to examine the morphology and size of the shadow, but angular resolution finer than the fringe spacing is desirable in order to produce

a clearer image that is more suitable for testing general relativity [1,31,32]. It is possible to create slightly superresolved images with CLEAN. (We define superresolution as $\lambda/(B\alpha)$, where λ is the observing wavelength, B is the projected length of the longest baseline, and $\alpha > 1$. Slightly superresolved ($\alpha \gtrsim 1$) reconstructed images are not uncommon, but the data do not contain enough information to reconstruct images with arbitrarily high superresolution ($\alpha \gg 1$).) However, MEM is better at squeezing more angular resolution out of a dataset [33].

Fourth, it is more natural to encode prior knowledge about the image into techniques that fit to the visibilities directly rather than CLEAN, which deconvolves the dirty beam from the dirty image using a "greedy algorithm" (i.e., at the peak in the dirty image at each iteration without considering the rest of the image). Even before taking any data on a source, very strong statements can be made about the range of images that are possible. For instance, pixels in a typical Stokes I image should be nonnegative, including many pixels that have no source flux in them at all. Typical images may have regions that vary smoothly and regions with sharp gradients, but flux is not distributed randomly among image pixels. Some constraints can be used with deconvolution methods, but it is simpler to add these as regularizers in methods that solve for an image in the data domain.

2.3. Lessons from Optical Interferometry

The imaging challenges faced by the EHT bear a strong resemblance to those confronted by the optical interferometry (OI) community [34]. Optical interferometers typically consist of a small number of telescopes, limiting the available (u, v) coverage. Atmospheric coherence times are orders of magnitude shorter at near-infrared and optical wavelengths, necessitating the use of closure phases or bispectra. Power spectra, rather than visibility amplitudes, are fundamental observables. In addition, some OI imaging targets, such as stellar disks, naturally present strong priors for the form of the reconstructed image.

Recognizing the inadequacy of contemporary image reconstruction techniques for OI data, the OI community has organized a biennial imaging contest [35–40]. Entries have spanned a wide range from adaptations of standard radio interferometric imaging techniques to completely new algorithms. Entries have included both deconvolution methods based on CLEAN and forward-imaging methods in which reconstructed images are evaluated in the data domain, the optimal image being the one that maximizes the likelihood of the data with a regularization penalty. In other words, the optimal image minimizes the sum of χ^2 and one or more additional terms that quantify prior expectations of a well-reconstructed image (e.g., sparseness or smoothness). Forward-imaging methods usually produce images that are judged to be closer to the simulated data presented in these imaging challenges.

Image reconstruction tests have demonstrated that the same forward-imaging algorithms developed by the OI community are superior to deconvolution methods for simulated EHT data [41]. Two OI imagers were tested: the BiSpectrum Maximum Entropy Method (BSMEM) and SQUEEZE [42,43]. Compared against multiscale CLEAN, both BSMEM and SQUEEZE produced higher-fidelity images with higher effective angular resolution [26].

2.4. New Imaging Algorithms for the EHT

The success of modern image reconstruction methods has encouraged a group within the EHT to investigate new algorithms that work with robust VLBI observables. Three of these methods are briefly described in this subsection.

2.4.1. Polarimetric MEM

Maximum entropy principles, which favor sparsity, apply equally well to polarimetric imaging. Early tests demonstrated that MEM is suitable for providing superresolution or for reconstructing extended emission structures [44].
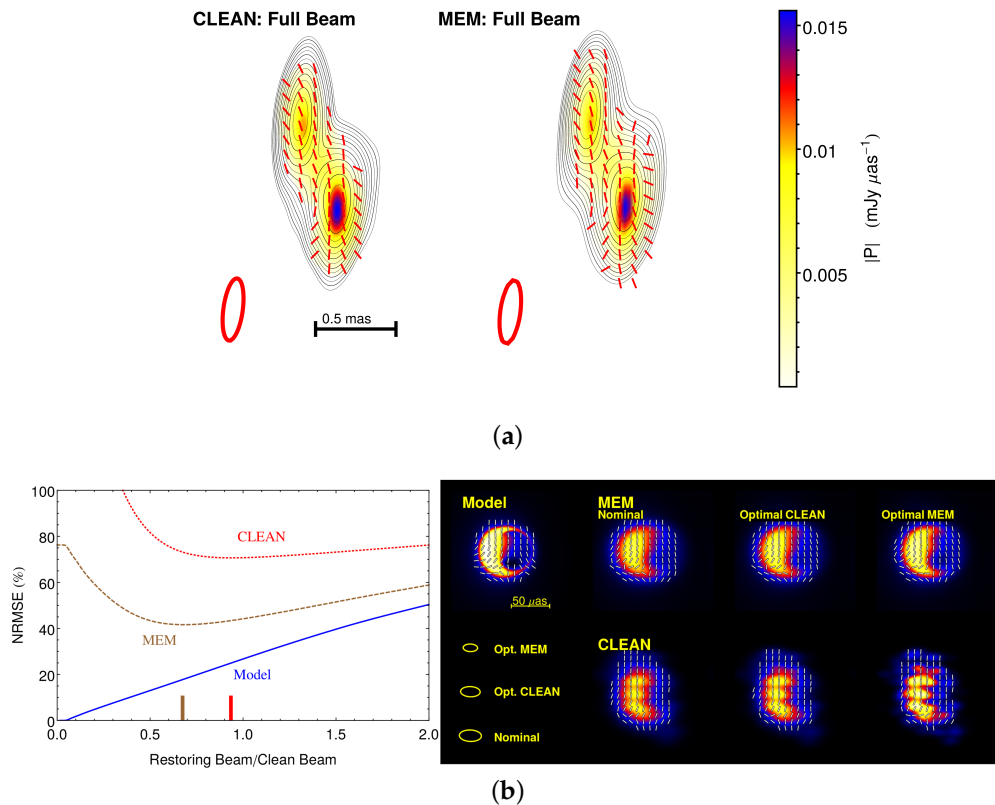
Figure 2. Validation and potential of polarimetric Maximum Entropy Method (MEM) imaging [45]. (**a**) Full-polarimetric images of 3C 279 from 7 mm Very Long Baseline Array (VLBA) data using CLEAN and MEM are nearly identical when the MEM image is convolved with the CLEAN beam; (**b**) Compared against a model image of Sgr A* at 1.3 mm, the normalized root-mean-square error of a polarimetric MEM reconstruction achieves its minimum at finer angular resolution than does CLEAN. MEM and CLEAN images reconstructed at the optimum beam sizes for each technique and the nominal beam size demonstrate that polarimetric MEM achieves superior resolution and image fidelity.

Polarimetric MEM imaging has recently been extended to handle robust VLBI observables, reconstructing Stokes I from bispectral data and Stokes Q and U from polarimetric ratios [45]. A variety of different regularizers have been explored beyond traditional total-intensity and polarimetric entropy terms, including regularizers that favor a prior image and reconstructions using ℓ_1 and ℓ_2 norms. At reasonably high signal-to-noise, the reconstructed image is not very sensitive to the choice of regularizer in either total intensity or polarization, and the method has been shown to produce good reconstructions even with 10% systematic uncertainties in visibility amplitudes. This technique has been validated on polarimetric 7 mm and 3 mm Very Long Baseline Array (VLBA) data, and it shows great promise for imaging the polarized structure in the inner accretion and outflow regions of Sgr A* and M87 (Figure 2).

2.4.2. Bi-Spectrum Sparse Modeling (BSSpM)

Compressed sensing techniques show promise for providing superresolution of sparse, compact structures. EHT simulations have demonstrated that compressed sensing using the Least Absolute Shrinkage and Selection Operator (LASSO), a regularizer based on the ℓ_1 norm, can reconstruct the shadow region of M87 quite well using visibility data [46]. BSSpM extends this method to work with closure phases rather than visibility phases [47].
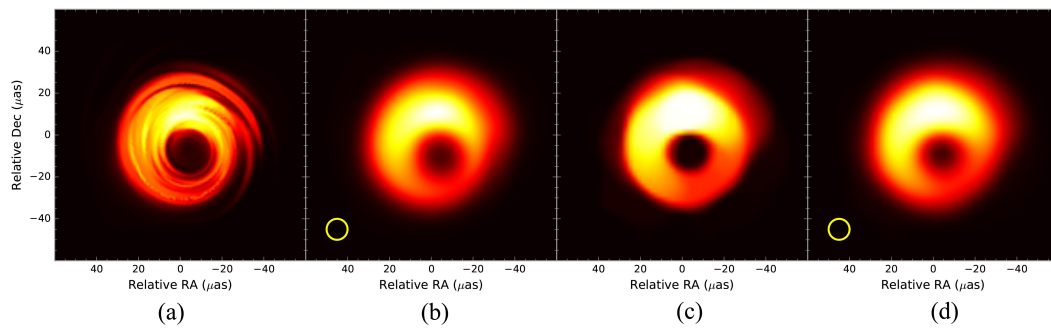
Figure 3. Bi-Spectrum Sparse Modeling (BSSpM) reconstruction of a disk-jet model of M87 at 1.3 mm. (**a**) The original model [48]; (**b**) The model convolved with a 10 μas Gaussian; (**c**) The BSSpM reconstruction of the image from simulated data [47]. The fringe spacing of the longest baseline is approximately 25 μas; (**d**) The BSSpM reconstruction convolved with a 10 μas Gaussian. BSSpM successfully recovers features of the model at a superresolution of 40% of the fringe spacing. A linear transfer function is used in all panels.

BSSpM also adds a second regularizer term for Total Variation (TV), which favors sparsity in the gradient of the image. Since TV regularization is edge-preserving, it is well suited to images with sharp boundaries between emitting and non-emitting regions, such as the inner edge of the black hole shadow or edge-brightened jets. Tests on simulated EHT data demonstrate that BSSpM has the potential to superresolve the black hole shadow region (Figure 3).

2.4.3. Continuous High-Resolution Image Reconstruction Using Patch Priors (CHIRP)

Since the problem of image reconstruction from sparse frequency measurements is ill-posed, we always have to inject some sort of information about what images look like, in the form of a regularizer or prior, in order to decide on a reconstructed image. However, it is not clear what this injected information should be, since black holes have not been imaged before. In addition, prior assumptions about what constitutes a good image may introduce biases into reconstructions. An alternative to hand-designing regularizers is to design data-driven priors. This provides the flexibility to easily encode different image assumptions into the imaging process by training the algorithm on different kinds of images.

CHIRP is an interferometric image reconstruction method that breaks images up into patches of pixels and models the structure of building blocks of different types of images [49]. A key insight is that not all arrangements of pixel brightnesses within a patch of a natural image are equally likely. For instance, natural images often contain some patches that are nearly uniform in intensity and others with a sharp gradient, but patches whose pixel intensities are random and uncorrelated are uncommon. Algorithms can be trained on large datasets of natural, celestial, or synthetic black hole images to determine the likelihood that any particular patch occurs. CHIRP solves for the image that is the best fit to the bispectral data, using the expected patch log likelihood as a regularizer.

CHIRP has been validated on a collection of images from the Boston University Blazar Group [50] (Figure 4). Under a comparison between imaging algorithms that was unsupervised (i.e., no user intervention was allowed to fine tune the algorithm for individual images), CHIRP tended to outperform CLEAN, BSMEM, and SQUEEZE, especially for datasets with lower signal-to-noise ratios and for reconstructing images of extended sources.
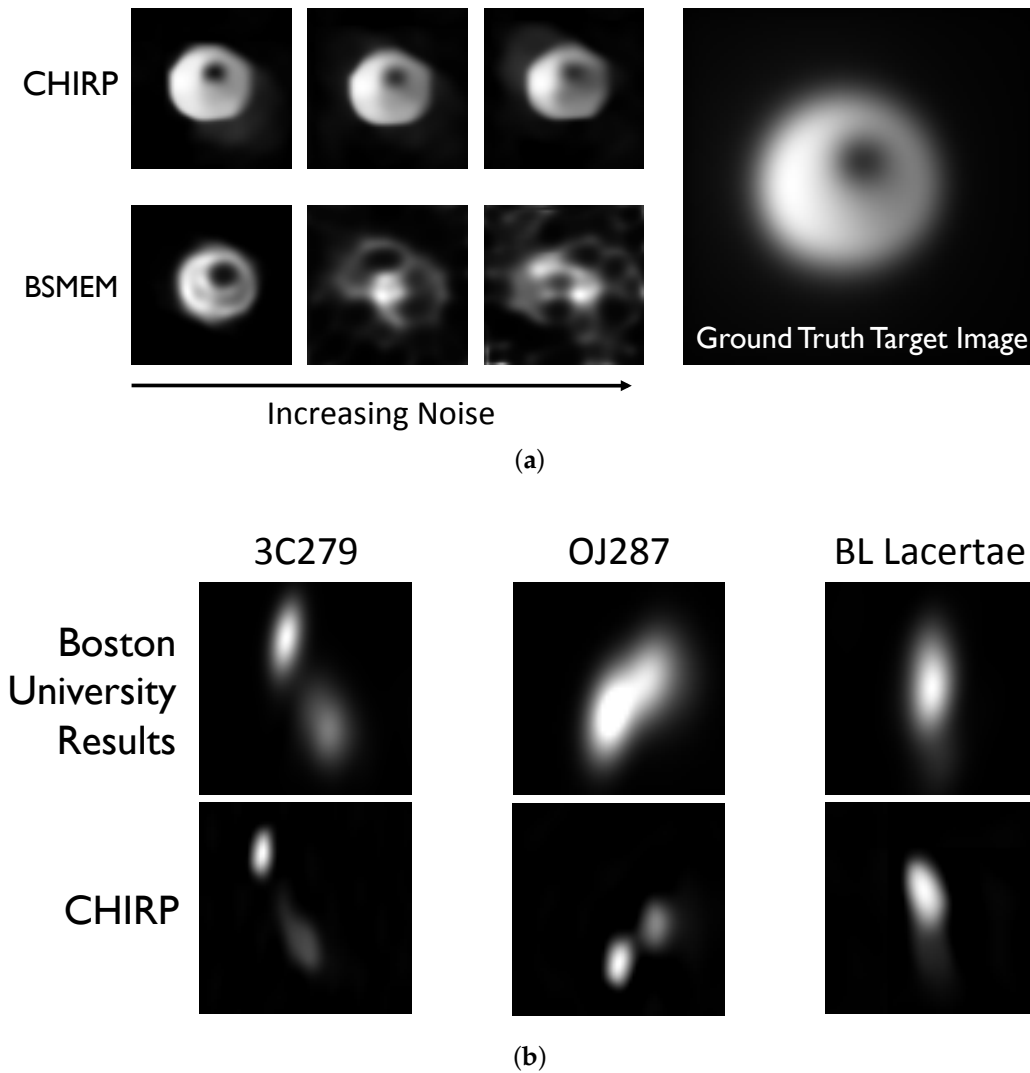
(**a**)

(**b**)

Figure 4. (**a**) Validation of Continuous High-Resolution Image Reconstruction using Patch Priors (CHIRP) on data from the Boston University Blazar Group demonstrating superresolution [49,50]; (**b**) Comparison of CHIRP (trained on natural images) and BiSpectrum Maximum Entropy Method (BSMEM) on reconstructing a black hole model image (courtesy A. Broderick) from simulated data. CHIRP is more robust as the signal-to-noise ratio of the simulated data is lowered. A linear transfer function is used in all panels.

2.5. Validation

It is important to validate the results of these and other new imaging methods. Inspired by the optical interferometry community, the EHT is organizing a series of imaging challenges (http://vlbiimaging.csail.mit.edu/imagingchallenge) to test the performance of new image reconstruction algorithms. The imaging challenges include real-world imperfections such as systematic noise due to miscalibration. The EHT imaging group is also testing algorithms on archival lower-frequency VLBI data in order to compare against published CLEAN images.

3. Summary

The Event Horizon Telescope has been able to probe Sgr A*, M87, and other AGN sources at very high angular resolution, addressing fundamental physical and astrophysical questions associated with

accreting black holes. Improvements in sensitivity and baseline coverage, notably the inclusion of ALMA in 2017, will significantly increase the capacity of the EHT to produce images.

New imaging techniques are being developed to use robust VLBI observables to make the most of the relatively sparse baseline coverage of the EHT. These techniques have broad applicability beyond the EHT (e.g., on longer-wavelength VLBI observations). Validation of these algorithms on real longer-wavelength VLBI data demonstrate their potential for reconstructed images with greater resolution and fidelity than currently provided by CLEAN. Observers using data from longer-wavelength VLBI arrays, such as the VLBA and GMVA, may find these methods useful.

Author Contributions: Vincent L. Fish wrote most of the article, with text and figure contributions from Kazunori Akiyama on BSSpM, from Katherine L. Bouman on CHIRP, and from Andrew A. Chael on Polarimetric MEM. All named authors of this work contributed to one or more of these imaging techniques (as listed in the references) and/or to the validation described in Section 2.5.

Conflicts of Interest: The authors declare no conflict of interest.

References

1. Doeleman, S.; Eric, A.; Backer, D.; Baganoff, F.; Bower, G.C.; Broderick, A.; Fabian, A.; Fish, V.; Gammie, C.; Ho, P.; et al. Imaging an Event Horizon: Submm-VLBI of a Super Massive Black Hole. 2009, arXiv:0906.3899.
2. Lu, R.-S.; Fish, V.L.; Weintroub, J.; Doeleman, S.S.; Bower, G.C.; Freund, R.; Friberg, P.; Ho, P.T.P.; Honma, M.; Inoue, M.; et al. Resolving the Inner Jet Structure of 1924−292 with the Event Horizon Telescope. *Astrophys. J. Lett.* **2012**, *757*, L14.
3. Lu, R.-S.; Fish, V.L.; Akiyama, K.; Doeleman, S.S.; Algaba, J.C.; Bower, G.C.; Brinkerink, C.; Chamberlin, R.; Crew, G.; Cappallo, R.J.; et al. Fine-Scale Structure of the Quasar 3C 279 Measured with 1.3 mm Very Long Baseline Interferometry. *Astrophys. J.* **2013**, *772*, 13.
4. Wagner, J.; Roy, A.L.; Krichbaum, T.P.; Alef, W.; Bansod, A.; Bertarini, A.; Güsten, R.; Graham, D.; Hodgson, J.; Märtens, R.; et al. First 230 GHz VLBI Fringes on 3C 279 Using the APEX Telescope. *Astron. Astrophys.* **2015**, *581*, A32.
5. Doeleman, S.S.; Weintroub, J.; Rogers, A.E.E.; Plambeck, R.; Freund, R.; Tilanus, R.P.J.; Friberg, P.; Ziurys, L.M.; Moran, J.M.; Corey, B.; et al. Event-Horizon-Scale Structure in the Supermassive Black Hole Candidate at the Galactic Centre. *Nature* **2008**, *455*, 78–80.
6. Doeleman, S.S.; Fish, V.L.; Schenck, D.E.; Beaudoin, C.; Blundell, R.; Bower, G.C.; Broderick, A.E.; Chamberlin, R.; Freund, R.; Friberg, P.; et al. Jet-Launching Structure Resolved Near the Supermassive Black Hole in M87. *Science* **2012**, *338*, 355–358.
7. Broderick, A.E.; Loeb, A.; Narayan, R. The Event Horizon of Sagittarius A*. *Astrophys. J.* **2009**, *701*, 1357–1366.
8. Broderick, A.E.; Narayan, R.; Kormendy, J.; Perlman, E.S.; Rieke, M.J.; Doeleman, S.S. The Event Horizon of M87. *Astrophys. J.* **2015**. *805*, 179.
9. Fish, V.L.; Doeleman, S.S.; Beaudoin, C.; Blundell, R.; Bolin, D.E.; Bower, G.C.; Chamberlin, R.; Freund, R.; Friberg, P.; Gurwell, M.A.; et al. 1.3 mm Wavelength VLBI of Sagittarius A*: Detection of Time-Variable Emission on Event Horizon Scales. *Astrophys. J.* **2011**, *727*, L36.
10. Fish, V.L.; Johnson, M.D.; Doeleman, S.S.; Broderick, A.E.; Psaltis, D.; Lu, R.-S.; Akiyama, K.; Alef, W.; Algaba, J.C.; Asada, K.; et al. Persistent Asymmetric Structure of Sagittarius A* on Event Horizon Scales. *Astrophys. J.* **2016**, *820*, 90.
11. Johnson, M.D.; Fish, V.L.; Doeleman, S.S.; Marrone, D.P.; Plambeck, R.L.; Wardle, J.F.C.; Akiyama, K.; Asada, K.; Beaudoin, C.; Blackburn, L.; et al. Resolved Magnetic-Field Structure and Variability Near the Event Horizon of Sagittarius A*. *Science* **2015**, *350*, 1242–1245.
12. Broderick, A.E; Fish, V.L.; Doeleman, S.S.; Loeb, A. Estimating the Parameters of Sagittarius A*'s Accretion Flow Via Millimeter VLBI. *Astrophys. J.* **2009**, *697*, 45–54.
13. Mościbrodzka, M.; Gammie, C.F.; Dolence, J.C.; Shiokawa, H.; Leung, P.K. Radiative Models of Sgr A* from GRMHD Simulations. *Astrophys. J.* **2009**, *706*, 497–507.

14. Dexter, J.; Agol, E.; Fragile, P.C.; McKinney, J.C. The Submillimeter Bump in Sgr A* from Relativistic MHD Simulations. *Astrophys. J.* **2010**, *717*, 1092–1104.

15. Chan, C.K.; Psaltis, D.; Özel, F.; Narayan, R.; Sądowski, A. The Power of Imaging: Constraining the Plasma Properties of GRMHD Simulations Using EHT Observations of Sgr A*. *Astrophys. J.* **2015**, *799*, 1.

16. Akiyama, K.; Lu, R.-S.; Fish, V.L.; Doeleman, S.S.; Broderick, A.E.; Dexter, J.; Hada, K.; Kino, M.; Nagai, H.; Honma, M.; et al. 230 GHz VLBI Observations of M87: Event-Horizon-Scale Structure during an Enhanced Very-High-Energy γ-ray State in 2012. *Astrophys. J.* **2015**, *807*, 150.

17. Gómez, J.L.; Lobanov, A.P.; Bruni, G.; Kovalev, Y.Y.; Marscher, A.P.; Jorstad, S.G.; Mizuno, Y.; Bach, U.; Sokolovsky, K.V.; Anderson, J.M.; et al. Probing the Innermost Regions of AGN Jets and Their Magnetic Fields with RadioAstron. I. Imaging BL Lacertae at 21 Microarcsecond Resolution. *Astrophys. J.* **2016**, *817*, 96.

18. Vertatschitsch, L.; Primiani, R.; Young, A.; Weintroub, J.; Crew, G.B.; McWhirter, S.R.; Beaudoin, C.; Doeleman, S.; Blackburn, L. R2DBE: A Wideband Digital Backend for the Event Horizon Telescope. *Publ. Astron. Soc. Pac.* **2015**, *127*, 1226–1239.

19. Plambeck, R.L.; Bower, G.C.; Rao, R.; Marrone, D.P.; Jorstad, S.G.; Marscher, A.P.; Doeleman, S.S.; Fish, V.L.; Johnson, M.D. Probing the Parsec-scale Accretion Flow of 3C 84 with Millimeter Wavelength Polarimetry. *Astrophys. J.* **2014**, *797*, 66.

20. Fish, V.; Alef, W.; Anderson, J.; Asada, K.; Baudry, A.; Broderick, A.; Carilli, C.; Colomer, F.; Conway, J.; Dexter, J.; et al. High-Angular-Resolution and High-Sensitivity Science Enabled by Beamformed ALMA. 2013, arXiv:1309.3519.

21. Tilanus, R.P.J.; Krichbaum, T.P.; Zensus, J.A.; Baudry, A.; Bremer, M.; Falcke, H.; Giovannini, G.; Laing, R.; van Langevelde, H.J.; Vlemmings, W.; et al. Future mmVLBI Research with ALMA: A European Vision. 2014, arXiv:1406.4650.

22. Högbom, J.A. Aperture Synthesis with a Non-Regular Distribution of Interferometer Baselines. *Astron. Astrophys. Suppl.* **1974**, *15*, 417–426.

23. Clark, B.G. An Efficient Implementation of the Algorithm "CLEAN". *Astron. Astrophys.* **1980**, *89*, 377–378.

24. Sault, R.J.; Wieringa, M.H. Multi-Frequency Synthesis Techniques in Radio Interferometric Imaging. *Astron. Astrophys. Suppl. Ser.* **1994**, *108*, 585–594.

25. Schwab, F.R. Relaxing the Isoplanatism Assumption in Self-Calibration; Applications to Low-Frequency Radio Interferometry. *Astron. J.* **1984**, *89*, 1076–1081.

26. Cornwell, T. Multiscale CLEAN Deconvolution of Radio Synthesis Images. *IEEE J. Sel. Top. Signal Process.* **2008**, *2*, 793–801.

27. Jennison, R.C. A Phase Sensitive Interferometer Technique for the Measurement of the Fourier Transforms of Spatial Brightness Distributions of Small Angular Extent. *Mon. Not. R. Astron. Soc.* **1958**, *118*, 276–284.

28. Rogers, A.E.E.; Hinteregger, H.F.; Whitney, A.R.; Counselman, C.C.; Shapiro, I.I.; Wittels, J.J.; Klemperer, W.K.; Warnock, W.W.; Clark, T.A.; Hutton, L.K.; et al. The Structure of Radio Sources 3C 273B and 3C 84 Deduced from the "Closure" Phases and Visibility Amplitudes Observed with Three-Element Interferometers. *Astrophys. J.* **1974**, *193*, 293–301.

29. Roberts, D.H.; Wardle, J.F.C.; Brown, L.F. Linear Polarization Radio Imaging at Milliarcsecond Resolution. *Astrophys. J.* **1994**, *427*, 718–744.

30. Cornwell, T.J.; Evans, K.F. A Simple Maximum Entropy Deconvolution Algorithm. *Astron. Astrophys.* **1985**, *143*, 77–83.

31. Johannsen, T.; Psaltis, D. Testing the No-hair Theorem with Observations in the Electromagnetic Spectrum. II. Black Hole Images. *Astrophys. J.* **2010**, *718*, 446–454.

32. Broderick, A.E.; Johannsen, T.; Loeb, A.; Psaltis, D. Testing the No-hair Theorem with Event Horizon Telescope Observations of Sagittarius A*. *Astrophys. J.* **2014**, *784*, 7.

33. Narayan, R.; Nityananda, R. Maximum Entropy Image Restoration in Astronomy. *Annu. Rev. Astron. Astrophys.* **1986**, *24*, 127–170.

34. Thiébaut, É. Principles of Image Reconstruction in Interferometry. *EAS Publ. Ser.* **2013**, *59*, 157–187.

35. Lawson, P.R.; Cotton, W.D.; Hummel, C.A.; Monnier, J.D.; Zhao, M.; Young, J.S.; Thorsteinsson, H.; Meimon, S.C.; Mugnier, L.M.; Le Besnerais, G.; et al. An Interferometry Imaging Beauty Contest. *Proc. SPIE* **2004**, *5491*, 886.

36. Lawson, P.R.; Cotton, W.D.; Hummel, C.A.; Baron, F.; Young, J.S.; Kraus, S.; Hofmann, K.-H.; Weigelt, G.P.; Ireland, M.; Monnier, J.D.; et al. 2006 Interferometry Imaging Beauty Contest. *Proc. SPIE* **2006**, doi:10.1117/12.670409.

37. Cotton, W.; Monnier, J.; Baron, F.; Hofmann, K.-H.; Kraus, S.; Weigelt, G.; Rengaswamy, S.; Thiébaut, E.; Lawson, P.; Jaffe, W.; et al. 2008 Imaging Beauty Contest. *Proc. SPIE* **2008**, doi:10.1117/12.788903.

38. Malbet, F.; Cotton, W.; Duvert, G.; Lawson, P.; Chiavassa, A.; Young, J.; Baron, F.; Buscher, D.; Rengaswamy, S.; Kloppenborg, B.; et al. The 2010 Interferometric Imaging Beauty Contest. *Proc. SPIE* **2010**, doi:10.1117/12.857066.

39. Baron, F.; Cotton, W.D.; Lawson, P.R.; Ridgway, S.T.; Aarnio, A.; Monnier, J.D.; Hofmann, K.-H.; Schertl, D.; Weigelt, G.; Thiébaut, E.; et al. The 2012 Interferometric Imaging Beauty Contest. *Proc. SPIE* **2012**, doi:10.1117/12.924907.

40. Monnier, J.D.; Berger, J.-P.; Le Bouquin, J.-B.; Tuthill, P.G.; Wittkowski, M.; Grellmann, R.; Müller, A.; Renganswany, S.; Hummel, C.; Hofmann, K.-H.; et al. The 2014 Interferometric Imaging Beauty Contest. *Proc. SPIE* **2014**, doi:10.1117/12.2057312.

41. Lu, R.-S.; Broderick, A.E.; Baron, F.; Monnier, J.D.; Fish, V.L.; Doeleman, S.S.; Pankratius, V. Imaging the Supermassive Black Hole Shadow and Jet Base of M87 with the Event Horizon Telescope. *Astrophys. J.* **2014**, *788*, 120.

42. Buscher, D.F. Direct maximum-entropy image reconstruction from the bispectrum. In Proceedings of the 158th International Astronomical Union (IAU) Symposium, Sydney, Australia, 11–15 January 1993; Volume 158.

43. Baron, F.; Monnier, J.D.; Kloppenborg, B. A Novel Image Reconstruction Software for Optical/Infrared Interferometry. *Proc. SPIE* **2010**, doi:10.1117/12.857364.

44. Holdaway, M.A.; Wardle, J.F.C. Maximum Entropy Imaging of Polarization in Very Long Baseline Interferometry. *Proc. SPIE* **1990**, doi:10.1117/12.23679.

45. Chael, A.A.; Johnson, M.D.; Narayan, R.; Doeleman, S.S.; Wardle, J.F.C.; Bouman, K.L. High Resolution Linear Polarimetric Imaging for the Event Horizon Telescope. *Astrophys. J.* **2016**, *829*, 1.

46. Honma, M.; Akiyama, K.; Uemura, M.; Ikeda, S. Super-Resolution Imaging with Radio Interferometry Using Sparse Modeling. *Publ. Astron. Soc. Jpn.* **2014**, *66*, 95.

47. Akiyama, K.; Kuramochi, K.; Ikeda, S.; Fish, V.L.; Tazaki, F.; Honma, M.; Doeleman, S.S.; Broderick, A.; Dexter, J.; Mościbrodzka, M.; et al. Imaging the Schwarzschild-Radii-Scale Structure of M87 with the Event Horizon Telescope Using Bi-Spectrum Sparse Modeling. *Astron. J.* **2016**, in press.

48. Dexter, J.; McKinney, J.C.; Agol, E. The Size of the Jet Launching Region in M87. *Mon. Not. R. Astron. Soc.* **2012**, *421*, 1517–1528.

49. Bouman, K.L.; Johnson, M.D.; Zoran, D.; Fish, V.L.; Doeleman, S.S.; Freeman, W.T. Computational imaging for VLBI image reconstruction. In Proceedings of the IEEE Conference on Computer Vision and Pattern Recognition, Seattle, WA, USA, 27–30 June 2016.

50. Jorstad, S.G.; Marscher, A.P.; Lister, M.L.; Stirling, A.M.; Cawthorne, T.V.; Gear, W.K.; Gomez, J.L.; Stevens, J.A.; Smith, P.S.; Forster, J.R.; et al. Polarimetric Observations of 15 Active Galactic Nuclei at High Frequencies: Jet Kinematics from Bimonthly Monitoring with the Very Long Baseline Array. *Astron. J.* **2005**, *130*, 1418–1465.